RSC Advances

PAPER

View Article Online
View Journal | View Issue

Cite this: *RSC Adv.*, 2024, **14**, 4153

Enhanced efficiency of photocatalytically synthesised Co^{3+}/Co^{2+}-incorporated CeO_2/SnO_2 nanocomposite and supercapacitor studies†

R. Silambarasan, Uttej Siva Sai Sundar Perisetti, S. Pavalamalar and K. Anbalagan *

The photochemical reduction approach, distilled H_2O with Pr^iOH as the solvent medium, was used to create and characterise the conversion of Co^{3+} to Co^{2+} integrated on CeO_2/SnO_2. The PXRD, IR, SEM, HR-TEM, VSM, and XPS results show that the materials generated have appropriate crystallisation form and retain the hollow spherical structure of Co–CeO_2/SnO_2. The performance of several UV-light energetic photocatalysts and the reaction pathways for inorganic complex degradation are addressed, emphasising the main elements contributing to their mineralisation. Reaction mechanisms, identification and quantification of degradation intermediates, and effects of reactive active species were described and analysed for each modelled target inorganic pollutant category. The ternary $(Co^{3+}/Co^{2+})/CeO_2/SnO_2$ materials were hypothesised to improve the photocatalytic activity by increasing the transport rate of e_{CB}^- impurities as a result of accelerating the practical separation of electron–hole (e^-/h^+) pairs. Then, it exhibits high cycling stability by successfully reducing the pulverisation of Co–CeO_2/SnO_2 electrode materials due to volume expansion and a high specific capacity of 827 F g^{-1}(1 A g^{-1}) while maintaining a high current density of 5 A g^{-1}. GCD and impedance spectroscopy studies were also carried out to analyse charge–discharge cycles and sample stability. This exceptional electrochemical performance suggests that Co–CeO_2/SnO_2 are promising for high-performance energy storage systems.

Received 20th November 2023
Accepted 18th December 2023

DOI: 10.1039/d3ra07947c

rsc.li/rsc-advances

1. Introduction

Industrialisation's economic growth is accompanied by significant environmental deterioration (*e.g.*, water and air pollution, climate change, loss of natural resources). The unregulated discharge of numerous hazardous substances, such as dyes, organic solvents, chemicals, petroleum products, heavy metals, and solid wastes, pollutes the environment.[1] For example, it can effectively reduce the recombination rate of photogenerated charge carriers in environmental remediation and the regenerative optical absorption of photocatalysts.[2] Because of their unique electrical and optical features, SnO_2 semiconductors have been extensively researched in photocatalysis, solar cells, and gas sensors. SnO_2-based photocatalysts gained the most attention because of their unique properties of high photo-oxidization, photostability, low cost, and non-toxicity.[3] SnO_2 and CeO_2 coupling can transfer specific electrons and holes from SnO_2 and CeO_2, simplifying electron–hole pair separation and increasing the photocatalytic activity of hybrid photocatalysts.[4] Heavy metal contamination is the most important environmental issue. Heavy metals require special attention because of their tenacity and permanence in the environment.[5–7] Recently, several heavy metal removal techniques have been thoroughly explored. These technologies include electrochemical processes, membrane filtration, adsorption, chemical precipitation, ion exchange, coagulation and flocculation, and flotation.[8,9] People's resource demand has increased dramatically as the industry has developed and living standards have improved, resulting in energy problems and environmental damage. In recent years, photocatalytic technology has demonstrated tremendous potential as a low-cost, environmentally friendly, and sustainably developed technology. Recent photocatalytic technologies, however, cannot satisfy industrial objectives.[10,11] CeO_2/SnO_2 is the most thoroughly researched semiconductor material because of its exceptional chemical and physical properties, including chemical inertness, non-toxicity, long-term stability, affordability, and enhanced photocatalytic efficacy.[12] Mobility is an important parameter for SnO_2, which is being explored intensively as a feasible transparent oxide n-type semiconductor. At ambient temperature, the mobility of electrons in bulk SnO_2 crystals varies from 70 to 260 $cm^2 V^{-1} s^{-1}$.[13] The n-type semiconductor

Department of Chemistry, Pondicherry University, Pondicherry, 605014, India. E-mail: kanuniv@gmail.com; Tel: +91 413 2654509

† Electronic supplementary information (ESI) available: Co–CeO_2/SnO_2 nanocomposite FT-IR spectra, UV-visible absorption spectra, Tauc plots, steady-state emission spectra, and lifetime analysis. See DOI: https://doi.org/10.1039/d3ra07947c

material cerium dioxide (CeO_2) has a band gap of around 3.0 eV and a dielectric constant between 23 and 52. While rare earth elements are usually trivalent (+3), cerium exists in trivalent (+3) and tetravalent (+4) states. Since the electronic structure of Ce^{4+} ([Xe]$4f^0$) is more stable than that of Ce^{3+} ([Xe]$4f^1$), the oxidation state of Ce^{4+} is assumed to be more stable than that of Ce^{3+} ([Xe]$4f^1$). Cerium oxide exists in two forms, with a continuous transformation between the oxygen-rich CeO_2 and the oxygen-deficient Ce_2O_3.[14,15] The fundamental characteristics of these charge transfer processes, such as charge creation, trapping, recombination, and electron and hole transport, are principally explored.[16] The Co-doped SnO_2 sample has the highest adsorption capacity and the smallest crystallite size dimension among the doped samples, resulting in the greatest specific surface area.[17,18] Since the valence of Co^{2+} is lower than that of Sn^{4+}, Co ions are used as doping agents to compensate for the absence of oxygen in the SnO_2 lattice. Consequently, with doping, the oxygen vacancy can be expected to decrease and SnO_2 to rearrange.[19] A co-precipitation process formed CeO_2, and it was functionalised by doping with transition metals, which are considered useful dopants to modify the properties of CeO_2 for catalytic application.[20] Supercapacitors have attracted much attention as energy storage devices due to their high specific power, quick charge–discharge rate, and extended cycle stability. The hunt for novel electrode materials to improve the specific capacitance of supercapacitors has been a focus of recent research.[21] Global demand for energy and associated devices is expanding, with high-efficiency energy storage device requirements increasing dramatically. As a result, there is much interest in finding possible answers to the energy dilemma, and much research has been conducted to that end.[22] Supercapacitors are unique from ordinary batteries in that they provide extremely efficient charge storage, rapid charge and discharge rates, ease of maintenance, and safety, making them particularly appealing for portable devices and automobiles. Under electrolytic circumstances, supercapacitors' performance is dictated by electrode composition and mechanical and physiochemical characteristics. Past research has investigated various materials and ways to realise high-energy and power density devices with high stability.[23] Due to their equivalent qualities, supercapacitors, or ultra-capacitors, occupy a position between regular capacitors and rechargeable batteries. Some benefits are long cycle life, rapid charge–discharge, and high power density. Supercapacitors have several advantages.[24] The synthesis of a Co–Mn composite using the sol–gel technique was reported, and it reached a specific 405 F g^{-1} at 5 mA cm^{-2}, demonstrating that the specific Mn capacitance increased with doping.[25]

In the present study, hydrothermally synthesised CeO_2/SnO_2 material nanocomposites were effectively investigated under UV illumination and showed a large surface area with potential functional dispersion for the photocatalytic process with the metal complex. The result of photosynthesis was (Co^{3+}/Co^{2+})/CeO_2/SnO_2. Cyclic voltammograms, charge–discharge curves, and electrochemical impedance spectra were used to study electrochemical characteristics.

2. Experimental

All the chemicals, including sodium nitrate, isopropyl alcohol, and ammonium thiocyanate from Hi-media Chemicals, were utilised without additional purification. A 6 W low-pressure mercury-vapour lamp from Heber Scientific (UV lamp) was used. The preparation of each composite was altered.

2.1. Synthesis of (Co^{3+}/Co^{2+})-incorporated CeO_2/SnO_2 composites

The photoreactor, a quartz glass reactor, was used to disperse 4.7786×10^{-4} M (25 mg) of the *cis*-[$Co(Phen)_2Cl_2$]Cl complex in 100 mL of plain water and distilled H_2O/Pr^iOH (70/30% (v/v)) solvent medium separately. The ionic strength of the solution was maintained by adding 10 mL of sodium nitrate (1 M) and 100 mg of CeO_2/SnO_2 catalyst and magnetic stirring. The dispersion's wavelength was 254 nm when irradiated by a UV lamp. The mixture was exposed to radiation for 20 minutes after being filtered and dried at room temperature. The samples obtained using plain water and those obtained using H_2O/Pr^iOH (70/30% (v/v)) are referred to in Table 5.

2.2. Sorption experiments

For the adsorption investigations, 100 mL of distilled H_2O/Pr^iOH (70/30% (v/v)) was dissolved in 4.761×10^{-4} M of *cis*-[$Co(Phen)_2Cl_2$]Cl and adjusted to pH 8 by adding sodium nitrate (1 M). The adsorbent CeO_2/SnO_2, CeO_2, and SnO_2 were diluted to approximately 100 mg. The resulting mixture was mixed for around 90 minutes at room temperature in a Technico warming water bath. At various time intervals, including 0, 5, 10, 15, 30, 45, 60, and 90 min, the adsorption ability of the adsorbent on Co(III) solution was examined. The adsorbent was spun apart and linked to the various time intervals to understand the metal ion's surface affinity. Electronic absorption spectroscopy analysis was performed on the filtrate.[24–28]

2.3. Photocatalytic analysis

The catalytic function of the photochemically recoverable binary composites (CeO_2/SnO_2, CeO_2, and SnO_2) from water and H_2O/Pr^iOH (70/30% (v/v)) systems was investigated. In a typical photocatalytic experiment, 4.761×10^{-4} M of *cis*-[$Co(Phen)_2Cl_2$]Cl, 100 mg of each catalyst, and organic reagents were tested in 100 mL of distilled water. After adding 1 M of sodium nitrate solution, the pH of 8 was changed, and photodegradation tests were carried out. After around 20 minutes of adsorption–desorption equilibrium, the catalyst samples were taken at various time intervals (0, 3, 6, 9, 12, 15, and 20 minutes) after irradiating with a 6 W low-pressure mercury lamp (Heber Scientific). The UV lamp produced 8.50×10^{17} photons per second of radiation. Following the illumination process, the catalyst was separated by centrifuging 5 mL of the solution collected at regular time intervals. Spectral analysis was used to quantify the concentration of Co(III) in the suspensions, and the Kitson technique was used to confirm the production of the Co(II) ion. A Shimadzu UV-2450 double-beam

spectrophotometer assessed the reduction of Co(III) ion solution utilising concentration variations and its usual absorption wavelength of 520 nm. The equation $X = [C_0 - C_t/C_0] \times 100$ was used to compute the photoefficiency, where X is the photo-efficiency, C_0 is the complex concentration at the start of the experiment, and C_t is the complex concentration at each time point.[29,30]

3. Results and discussions

3.1. XRD analysis

X-ray diffractogram analysis (XRD) was used to examine the crystal structure of the obtained pure CeO_2/SnO_2, CeO_2, and SnO_2 nanocomposites with various (Co^{3+}/Co^{2+}) doping levels. The usual patterns are depicted in Fig. 1. The identifiable peaks from these diffraction patterns were six (Co^{3+}/Co^{2+})/CeO_2 peaks (JCPDS no. 48-1548) and eight (Co^{3+}/Co^{2+})/SnO_2 peaks (JCPDS no. 002-1340).[31] The samples had the same diffraction peaks, as the graph shows. Logically, all the produced (Co^{3+}/Co^{2+})/CeO_2/SnO_2 composites have tetragonal rutile structures, as shown by the standard (JCPDS no. 41-1445).[32,33]

Interestingly, all samples showed the same characteristic peaks, proving that the crystal structure is independent of the Co doping concentrations of less than 2%; no Co peaks could be seen. The Scherrer equation $D = 0.9/(\cos\theta)$ was used to obtain the average mean crystallite size. Using this equation, the average crystallite size of (Co^{3+}/Co^{2+})/CeO_2/SnO_2, (Co^{3+}/Co^{2+})/CeO_2, and (Co^{3+}/Co^{2+})/SnO_2 samples was 15.51, 7.05, and 8.89 nm, respectively. Table 1 shows the average crystalline samples. Smaller particles were distributed more evenly and uniformly in a solvent mixture than in water.

3.2. Raman analysis

Photochemically produced samples' Raman spectra of Co–CeO_2/SnO_2, Co–CeO_2, and Co–SnO_2 are shown in Fig. 2. In this section, the vibration modes of samples taken from systems containing distilled H_2O/Pr^iOH (70/30% v/v) are characterised. Fluorite cubic-structured nano-CeO_2 belongs to the $Fm\bar{3}m$ space group with O_h

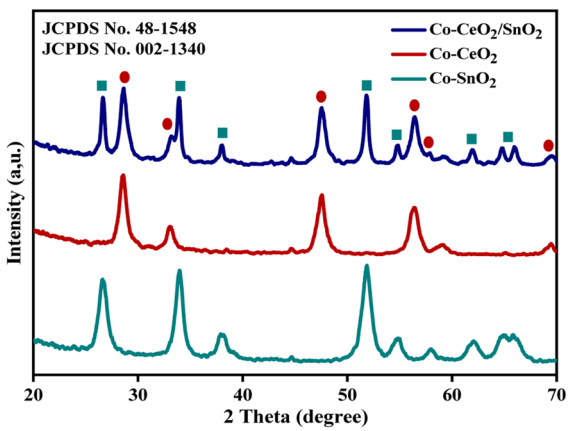

Fig. 1 X-ray diffraction pattern of Co–CeO_2/SnO_2, Co–CeO_2, and Co–SnO_2 nanospheres.

Table 1 Various spectroscopic measurements of the prepared nanomaterials

Sample	Raman mode[a] (cm^{-1})	Average crystallite size[b] (nm)	DRS spectrum[c]		Photoluminescence spectrum[d]			Average life time[e] (ns)
			Absorption edge (nm)	Band gap energy (eV)	λ_{emi} (nm)	Intensity $\times 10^3$ cps	λ_{exc} (nm)	
Co–CeO_2/SnO_2	464	15.51	340	3.1	399	17.372	300	30
	640				466	13.331		
	778				518	8.911		
Co–CeO_2	466	7.05	330	3.03	399	12.296	300	29
					463	7.389		
					517	3.497		
Co–SnO_2	478	8.89	300	3.4	398	12.973	300	29
	633				480	10.205		
	771				518	9.842		

[a] Raman spectral data. [b] Recorded at laser power at 784 nm; calculated by the Scherrer equation from XRD measurements. [c] UV-vis absorption spectra band gap energy. [d] Photoluminescence spectra. [e] Decay data average lifetime.

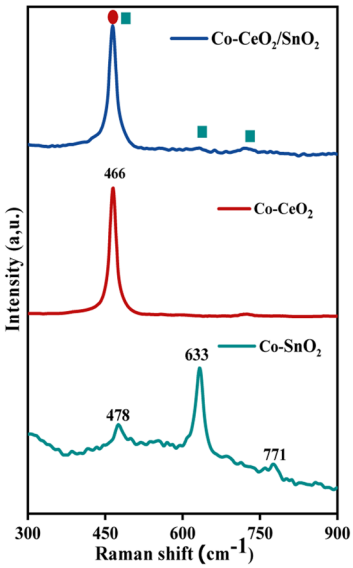

Fig. 2 Raman spectra of Co–CeO_2/SnO_2, Co–CeO_2, and Co–SnO_2 nanospheres using an excitation laser source of 784 nm ranging between 200 and 800 cm^{-1}.

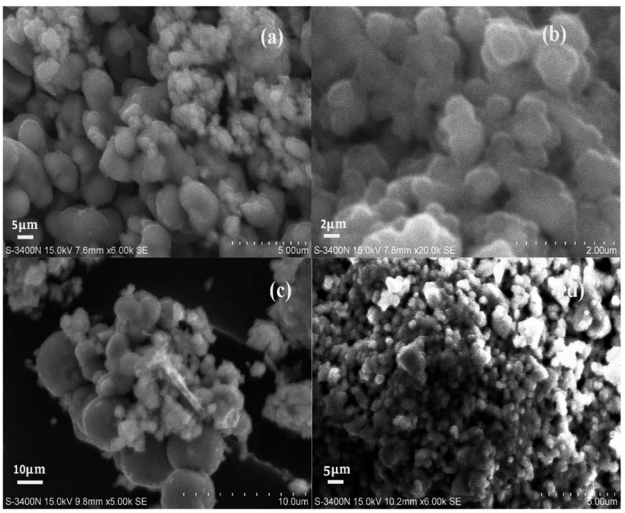

Fig. 3 SEM images of (a) nano-Co–CeO_2 magnification at 10 µm; (b) nano-Co–SnO_2 magnification at 10 µm; (c) Co–CeO_2/SnO_2 composite magnification at 10 µm; and (d) Co–CeO_2/SnO_2 composite magnification at 20 µm.

and exhibited peaks at 464 cm^{-1}. The band is at 464 cm^{-1} and is associated with the transverse F_{2g} vibration mode.[33–35] Tetragonal rutile-structured nano-SnO_2 belongs to the $P4_2/mm$ space group with D_{4h} and exhibits peaks at 478, 633, and 771 cm^{-1}, which are associated with the transverse A_{1g}, B_{1g}, B_{2g}, and E_g vibration modes. The peaks at 478 and 634 cm^{-1} are defined as translational (E_g) and symmetric (A_{1g}) modes, respectively; the peak at 771 cm^{-1} is classed as the asymmetric (B_{2g}) mode. Raman methods allow spectral patterns of nanoscale CeO_2, SnO_2, and CeO_2/SnO_2 nanocomposites with Co^{3+}/Co^{2+} impurities.[36,37]

3.3. UV-vis spectral analysis

The UV-vis absorption spectra and Tauc plots were acquired to explain the optical properties of Co–CeO_2/SnO_2, Co–CeO_2, and Co–SnO_2, as shown in Fig. S2.† The absorption edge was observed at 340, 330, and 300 nm, and the optical band gap was 3.1, 3.03, and 3.4 eV. The optical absorption curves of all samples were fitted at the absorption edges using the Tauc/David–Mott model to obtain the bandgap (E_g).[38,39] According to the findings, interface imperfections in agglomerated nanoparticles lowered the bandgap energy and improved the separation and transportation of photogenerated electron–hole (e^-/h^+) pairs for photocatalytic activity.[40,41]

3.4. SEM and TEM analysis

SEM images of 2% Co-doped CeO_2/SnO_2, CeO_2, and SnO_2 nanocomposites are shown in Fig. 3. The Co–CeO_2/SnO_2 particles have an average diameter of 40 nm and are uniform in size and shape. A spherical composite measuring 10 mm in length and 1 to 1.5 mm in diameter results from the hydrothermal process. When co-doping levels were less than 2%, there were no discernible forms or sizes.[42,43]

The HR-TEM image in Fig. 4a demonstrates an interconnected, highly crystalline agglomeration consistent with the SEM findings. The magnified HR-TEM image in Fig. 4b exhibits a clear lattice fringe with an interplanar distance of 0.26 and 0.25 nm, corresponding to the (111) and (110) Co-doped CeO_2/SnO_2 planes. The result suggests that the particle size was about 25 nm, close to the XRD analysis value. Further, the selected area electron diffraction (SAED) pattern in Fig. 4c reveals the diffracted rings of Co-doped CeO_2/SnO_2.[43,44]

3.5. Photoluminescence and lifetime studies

The fluorescence spectra of all the samples were taken at an excitation wavelength of 300 nm. As shown in Fig. S3,† it is evident that the PL intensity of ternary Co–CeO_2/SnO_2 nanocomposites is significantly lower than that of Co–CeO_2 and Co–SnO_2. This results in low charge carrier recombination and a long lifetime of electron–hole pairs, improving the photocatalytic activity. Strong emission at 400 nm (12.76×10^3) and reduced intensity peaks at 468 and 528 nm lessen the possibility of self-trapped excitons undergoing radiative recombination, enhancing the charge separation process. The peak at 468 nm appeared with low intensity and could be attributed to the characteristic near-band-edge emission. The radiation-induced transition from oxygen vacancies to the valence band with a single trap electron of Co–CeO_2/SnO_2 can be attributed to the peak at 528 nm.[45] The samples' intensities can be arranged in the following order: Co–CeO_2/SnO_2 > Co–CeO_2 > Co–SnO_2. Compared to an aqueous medium, adding an H_2O/Pr^iOH solvent mixture slightly increases the incorporation of Co^{3+}/Co^{2+} ions into the mixtures. The Co^{3+}/Co^{2+} ion provides a new energy level to lessen the recombination of electron–hole pairs. Due to the differing Fermi levels and electronic band structures of Co^{3+}/Co^{2+}-integrated CeO_2/SnO_2 semiconductors, the Schottky barrier can significantly impact the photo-induced

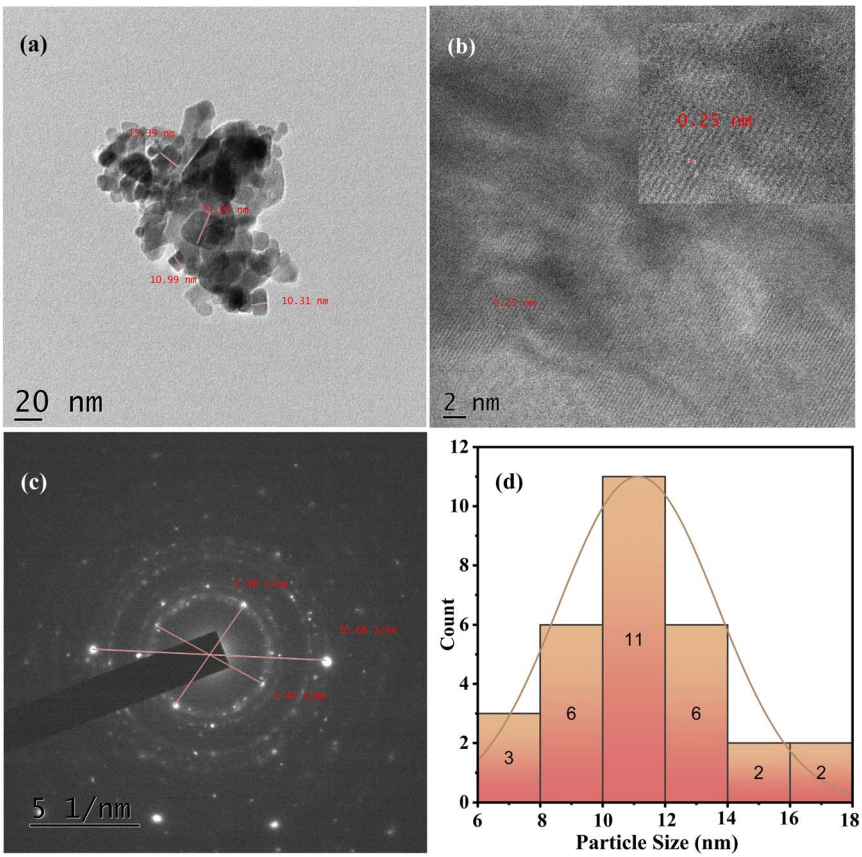

Fig. 4 (a) TEM micrograph of Co–CeO_2/SnO_2 nanocomposite and its corresponding magnification at 20 nm; (b) lattice fringes; (c) SAED pattern; and (d) particle size distribution histogram.

charge carriers.[46] For Co–CeO_2/SnO_2 composites, the PL intensities substantially decreased; this can be explained by reduced charge carrier transfer and charge carrier recombination rate within the heterojunction. The degradation process of the nanocomposite samples of Co–CeO_2/SnO_2, Co–CeO_2, and Co–SnO_2 made from plain water and H_2O/Pr^iOH (70/30% v/v) is shown in Fig. S4.† The triexponential equation ($I = \Sigma nA_n \exp(-t/\tau_n)$), where A_n denotes the amplitude of the component and τ_n represents the component's lifetime, fits all of the data quite well. The average PL lifespan may be calculated using the equation $\tau_{avg} = (B_1\tau_1^2 + B_2\tau_2^2 + B_3\tau_3^2)/(B_1\tau_1 + B_2\tau_2 + B_3\tau_3)$. According to the equation, the decay sample of plain water and H_2O shows no apparent changes: system H_2O/Pr^iOH (70/30% v/v). Using the equation in Table 1, the decay time of the relative percentage of the three components for Co–CeO_2/SnO_2, Co–CeO_2, and Co–SnO_2 is 30, 29, and 29 ns. As a result, heterojunction material maintains lifespan and suppresses electron and hole recombination, consistent with photocatalytic performance.

3.6. Magnetic properties

The magnetic characteristics of low amounts of Co^{3+}/Co^{2+} contained in CeO_2/SnO_2, CeO_2, and SnO_2 were investigated by vibrating the sample magnetometer at room temperature. Fig. 5 shows the magnetisation curves of samples from plain water and H_2O/Pr^iOH (70/30% v/v). All of the samples displayed ferromagnetic activity. In the samples, oxygen or cation vacancies might be due to the reorientation caused by the spin–spin connection of Ce–O and Sn–O dipoles.[47,48]

Table 2 shows the saturation magnetisation of Co–CeO_2/SnO_2 at 12.1785 emu g^{-1}, Co–CeO_2 at 5.0672 emu g^{-1}, and Co–SnO_2 at 9.6529 emu g^{-1} in H_2O/Pr^iOH (70/30% v/v). The higher

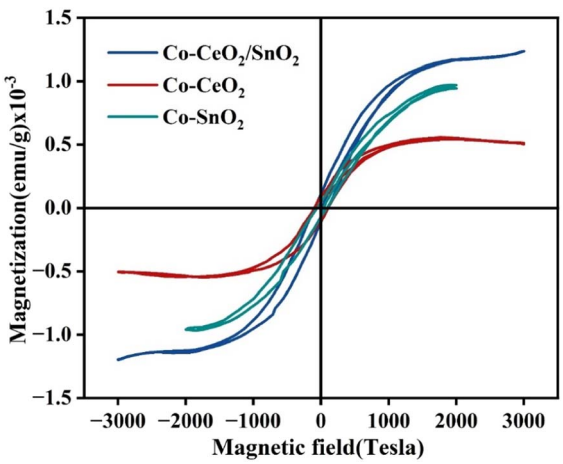

Fig. 5 Room-temperature M–H hysteresis loops recorded for Co–CeO_2/SnO_2 nanocomposite, nano-Co–CeO_2, and nano-Co–SnO_2.

Table 2 Vibrating sample magnetometer of Co–CeO_2/SnO_2, Co–SnO_2 nanocomposite, and Co–CeO_2 nanoparticles at room temperature

Sample	Hc, Oe	M_R, $cm^3\ mol^{-1} \times 10^{-4}$	M_s, (emu g^{-1}) $\times 10^{-4}$
Co–CeO_2/SnO_2	99.72	1.1223	12.1785
Co–CeO_2	95.08	0.9313	5.0672
Co–SnO_2	71.89	0.5921	9.6529

the Co addition in ternary compounds, the lower the magnetic concentration compared to binary components. Furthermore, the Co ion-doped samples form a new interface to affect the non-magnetic CeO_2 and SnO_2 nanoparticles. Nevertheless, Co ion incorporation into CeO_2/SnO_2 preserved enough magnetism that an external magnetic field would still attract them and readily remove the catalyst.

3.7. FT-IR analysis

FT-IR spectroscopy may disclose the nature of the chemical interactions of the metal-oxide link in composites, as shown in Fig. S1,† which was produced from a combination of H_2O/Pr^iOH (70/30% v/v). The hydroxyl group of the adsorbed atmospheric water molecule in each sample exhibits stretching and bending vibrations, represented by the various modes at 340 cm^{-1}, 2925 cm^{-1}, and 1622 cm^{-1}, respectively. The 526 cm^{-1} modes correspond to the Ce–O–Ce stretching vibrations of Co–CeO_2 samples. The peaks at 670 cm^{-1} are attributed to the Sn–O and Sn–O–Sn stretching vibrations of the Co–SnO_2 binary phases. The coexistence of Ce–O–Sn vibrations in the third phase of Co–CeO_2/SnO_2 is attributed to a large region spanning from 423 to 750 cm^{-1}.[26,27]

3.8. XPS analysis

The Co–CeO_2/SnO_2 sample ternary phase high-resolution XPS survey spectrum is presented in Fig. 6a, where the components Ce, Sn, O, and Co can be easily detected. In Fig. 6b, the observed binding energies at 902.32 eV are compatible with Ce^{4+} ($2p_{5/2}$) and the peaks at 884.14 eV are consistent with Ce^{4+} ($2p_{3/2}$).[27] Fig. 6c depicts the Sn 3d scans of the Co–CeO_2/SnO_2 sample, which exhibit two peaks associated with Sn^{4+} ($3d_{5/2}$) and Sn^{4+} ($3d_{3/2}$), with binding energies of 496.19 and 487.60 eV, respectively. The high-resolution spectra of the O 1s spectrum were deconvoluted into two peaks with binding energies of 529.19 and 531.79 eV, commonly assigned to lattice O_2 ions of the CeO_2 and SnO_2 surfaces, respectively. Furthermore, high-resolution spectra of Co 2p (Fig. 6e) may be obtained from two peaks with binding energies of 807.3 eV (Co^{2+}, $2p_{3/2}$) and 785.00 eV (Co^{3+}, $2p_{1/2}$), suggesting the presence of the reduced form of the Co^{2+} ion in the sample.[49,50]

4. Adsorption experiments

Adsorbents such as Co–CeO_2/SnO_2, Co–CeO_2, and Co–SnO_2 have 26, 12, and 14% surface interactions, respectively. The rate constant of the nanocomposites in water and H_2O/Pr^iOH (70/30% v/v) is greater than that of the bare components. The adsorbent's adsorption capacity did not change at 90 minute intervals, indicating that the adsorbent surface is saturated with active sites. At low pH 8, the number of accessible vacant or

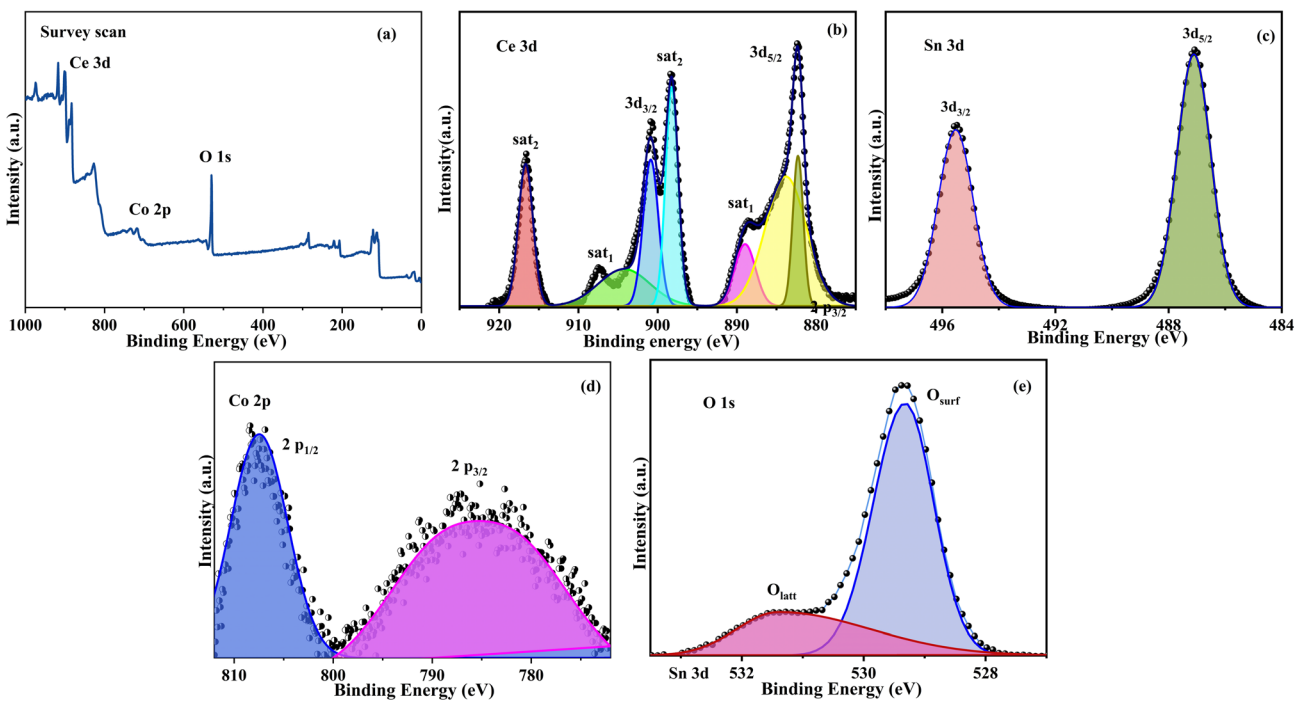

Fig. 6 XPS of Co–CeO_2/SnO_2 nanocomposite. (a) Survey scan; (b) Ce 3d; (c) Sn 3d; (d) O 1s; (e) Co 2p. The chemical environment and composition of Co–CeO_2/SnO_2 composite surface species were studied using XPS.

binding sites for the adsorption of heavy metal ions increased due to better surface contact of the ternary nanocomposite. An ideal concentration of the heavy metal ion was utilised in the adsorbent to remove it more effectively; when the concentration of Co(III) was raised, the effectiveness dropped. This might cause an increased likelihood of a collision between the heavy metal ion and the adsorbent.[30]

5. Photocatalytic activity

Size, shape, photogenerated electron species, decay time, and heterojunction materials' electrical and interfacial charge transfer affect photocatalytic activity. After a 20 min dark adsorption–desorption process, Co(III) reduction of H_2O/Pr^iOH (70/30% v/v) was used to test the photocatalytic activity of Co–CeO_2/SnO_2, Co–CeO_2, and SnO_2 components and was found to be 71, 45, and 42%, respectively. A pseudo-first-order kinetics of Co(III) to Co(II) decomposition curves was revealed in the presence of ternary nanocomposite catalysts under 254 nm UV light irradiation at room temperature (Fig. 7 and Table 3).[30,51,52]

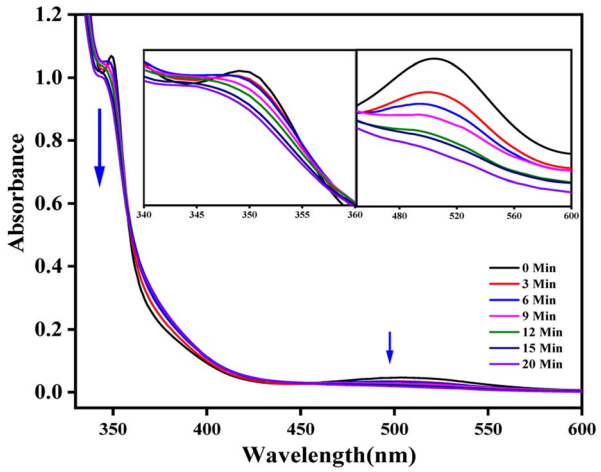

Fig. 7 Electronic absorption spectra of time-dependent photodegradation (254 nm) of *cis*-$[Co(phen)_2Cl_2]Cl$ complex in Co–CeO_2/SnO_2 in 30% IPA–water mixture.

5.1. Proposed photo-mechanism

Reports show that photo-excited charge carriers pass the heterogeneously structured interface in the Co–CeO_2/SnO_2 composite process. For (Co^{3+}/Co^{2+}) migration, understanding the band gap of coupled CeO_2 and SnO_2 is crucial; additionally, the splitting of electron/hole pairs in photocatalysis, with a focus on the photo-mechanism.

$$E_{VB} = \chi - E^e - \tfrac{1}{2}E_g \quad (1)$$

$$E_{CB} = E_{CB} - E_g \quad (2)$$

where E_{CB} and E_{VB} are the CB and VB band edge potential, respectively, and χ is the electronegativity of the semiconducting materials. When exposed to light, the photogenerated electrons in the CeO_2 and SnO_2 VB levels are excited to their CB levels, leaving holes in the VB levels of the corresponding catalysts. The intercalated Co^{3+} ion can transfer and reduce the excited electrons in the CB of SnO_2 by lowering them. SnO_2 has a band potential at the CB level significantly lower than the reference potential for Co^{3+}/Co^{2+} (0.77 eV *vs.* NHE). An electron donor and an acceptor are connected *via* an intercalated (Co^{3+}/Co^{2+}) ion in the compound. The generated Co^{2+} reacting with H_2O_2 completes the cycle to form $^{\bullet}OH$ radicals and convert them to Co^{3+}. Upon exposure to light, the excited electron of SnO_2 CB states is transferred to Co(III) and then reduced to Co(II). SnO_2 has a lower CB (0.11 eV) than the typical $O_2/^{\bullet}O_2$ (0.046 eV) oxidation potential. As a result, O_2 can be generated as $O_2/^{\bullet}O_2$ by photocatalytic electrons on the surface of

Table 3 Photoefficiencies of nanomaterials at various IPA–water mixtures

		Photoefficiency (%)								
		Time (min)								
Reaction conditions	Catalyst	0	3	6	9	12	15	20	Rate constant (k, s^{-1})	R^2
Aqueous	CeO_2/SnO_2	0	2	10	15	17	19	33	0.0182	0.9097
	CeO_2	0	3	7	10	13	16	19	0.0135	0.9429
	SnO_2	0	3	9	11	15	19	21	0.0236	0.9030
10% Pr^iOH in water	CeO_2/SnO_2	0	4	14	29	33	41	44	0.0313	0.9289
	CeO_2	0	5	10	18	28	33	37	0.0306	0.9354
	SnO_2	0	8	17	21	27	30	33	0.0213	0.9629
20% Pr^iOH in water	CeO_2/SnO_2	0	5	10	28	40	41	51	0.0406	0.9502
	CeO_2	0	5	10	21	33	37	41	0.0358	0.9383
	SnO_2	0	9	17	23	28	31	38	0.0236	0.9751
30% Pr^iOH in water	CeO_2/SnO_2	0	27	36	51	56	62	71	0.0625	0.9795
	CeO_2	0	10	15	32	37	41	45	0.0355	0.9160
	SnO_2	0	12	25	28	33	41	42	0.0313	0.9366
40% Pr^iOH in water	CeO_2/SnO_2	0	6	12	25	34	43	51	0.0383	0.9113
	CeO_2	0	5	9	17	32	36	40	0.0342	0.9315
	SnO_2	0	6	11	19	26	29	36	0.0236	0.9756

CeO_2. Meanwhile, photo-generated holes can be formed on the surface of SnO_2 (2.86 eV) to convert OH^- to $OH^\bullet$ (1.99 eV). Photo-generated electrons can be excited but ineffectively localised in the VB states of the CeO_2 heterostructured interface in the absence of electron mediator Co ions.[30] The plausible photo-mechanism is as follows:

$$CeO_2/(Co^{3+}/Co^{2+})/SnO_2 + h\nu \rightarrow CeO_2(e^- + h^+)/(Co^{3+}/Co^{2+})/SnO_2 \quad (3)$$

$$CeO_2(e^- + h^+)/(Co^{3+}/Co^{2+})/SnO_2 \rightarrow CeO_2(h^+)/(Co^{3+}/Co^{2+})(e^-)/SnO_2 \quad (4)$$

$$CeO_2(h^+)/(Co^{3+}/Co^{2+})(e^-)/SnO_2 \rightarrow CeO_2(h^+)/(Co^{3+}/Co^{2+})/SnO_2(e^-) \quad (5)$$

$$SnO_2(e_{VB}{}^-) \rightarrow SnO_2(e_{CB}{}^-) \quad (6)$$

$$SnO_2(e_{CB}{}^-) + O_2 \rightarrow {}^\bullet O_2{}^- \quad (7)$$

$$CeO_2(h^+) + OH^- \rightarrow CeO_2 + {}^\bullet OH \quad (8)$$

$$CeO_2(h^+) + {}^\bullet OH + {}^\bullet O_2{}^- + \rightarrow CeO_2 + O_2 + H_2O \quad (9)$$

$${}^\bullet O_2{}^- + H_2O \rightarrow {}^\bullet O_2H + OH^- \quad (10)$$

$${}^\bullet O_2H + H^+ + e_{CB}{}^- \rightarrow H_2O_2 \quad (11)$$

$$e_{CB}{}^- + H_2O_2 \rightarrow {}^\bullet OH + OH^- \quad (12)$$

$$Co^{2+} + H_2O_2 \rightarrow Co^{3+} + {}^\bullet OH + OH^- \quad (13)$$

$$Co^{3+} + H_2O_2 \rightarrow Co^{2+} + {}^\bullet O_2H + H^+ \quad (14)$$

Reactions (3)–(14) imply the possible pathway of the photocatalytic process.

6. Electrochemical studies

Nickel foam (20 mm × 10 mm × 1 mm) was sonicated by washing in ethanol (20 mL), 2 mM HCl aqueous solution (20 mL), and deionised water (20 mL) for a total of 30 min. In the initial stage of working electrode preparation, activated carbon black and polyvinylidene fluoride (PVDF) were added to the Co–CeO_2/SnO_2 composite electrodes in a ratio of 80 : 10 : 10. After 30 min of solution, the mixture was triturated with *N*-methyl-2-pyrrolidone to form the desired emulsion. After that, Ni foam working electrodes were prepared and dried at 80 °C for 12 hours to provide an emulsion coating with an area of 1 mm × 1 mm. Ag/AgCl and platinum plates were used as the reference electrode and the counter electrode in a three-electrode configuration, and the mass difference of all prepared electrodes was 2 mg.[53]

The prepared Co–CeO_2/SnO_2 nanocomposite was subjected to cyclic voltammetry tests using an aqueous electrolyte of 4 M KOH at a potential range of 0 to 0.5 V. The capacitive characteristics of the samples were investigated at CV from 3 to 15 mV s^{-1}, as shown in Fig. 8a.[54] The Co–CeO_2/SnO_2 nanocomposite exhibits good elasticity and stability; 1 A g^{-1} by the uniform shape of the CV curve calculates the maximum specific capacitance values for the Co–CeO_2/SnO_2 nanocomposite of 692 F g^{-1}.

The obtained samples were exposed to galvanostatic charge–discharge experiments in a potential window of 0 to 0.46 V from 1 to 5 A g^{-1} (Fig. 8b). The specific capacitance decreases with increasing current density,[55] probably due to fewer active sites in the reaction; its maximum value is observed at 1 A g^{-1}. This can be caused by ions sticking to the surface of the electrode, ions diffusing improperly, or insufficient charge transfer within the electrode. According to GCD curve calculations, the maximum specific capacitance values for Co–CeO_2/SnO_2 nanocomposite are 827 F g^{-1}. GCD shows that the discharge time of the samples is higher than that of the Co–CeO_2/SnO_2 nanocomposite, proving the material's superior capacitive properties. Fig. 8d shows the specific capacitance and current density from 1 to 5 A g^{-1} determined from GCD and CV. The Ragone plot in Fig. 8e is similar to the plot of ordinary supercapacitors. It enables the fabrication of supercapacitor devices because significant power and energy density have been achieved.[56–58]

Electrochemical impedance spectroscopy (EIS) measurements were performed at 5 mV in the frequency range from 0.001 Hz to 100 kHz to understand the charge transfer mechanism at the electrode–electrolyte interface. Fig. 8c shows the Nyquist plot of the Co–CeO_2/SnO_2 sample with its equivalent circuit. The components of the comparable circuit are Warburg resistance W, charge transfer resistance R_c, leakage resistance R_{lk}, constant phase element Q, and solution resistance element R_s. The electrode–electrolyte interface consists of a linear zone without a semicircle, representing a minimum charge transfer resistance. A change in low impedance values may result in specific capacitance observed from the Nyquist plots after 750 cycles. Although there is a typical reduction in specific capacitance after a few cycles, Co–CeO_2/SnO_2 nanoparticles have a higher specific capacitance than other materials. For the Co–CeO_2/SnO_2 samples, the capacity retention was determined to be 50%.[59] Table 4 lists values for specific capacitance, power density, and ESI.

A three-electrode system measures Mott–Schottky (MS) layers at the electrode/electrolyte interface; a standard saturated Ag/AgCl is the reference electrode, and a Pt plate is the counter electrode. The objective was to determine the conductivity type and donor concentration of electrochemically deposited Co–CeO_2/SnO_2 Ni foam. Using the MS equation, we estimated the CB of Co–CeO_2/SnO_2 Ni foam.[60]

$$C_{SC} = \pm \frac{2}{q\varepsilon\varepsilon^0 N_d}\left(V - V_1 + \frac{kT}{q}\right)$$

(+ denotes n-type and − denotes p-type), where C is the space-charge region's capacitance, q is its electron charge (1.602×10^{-19} C), and ε is its relative permittivity ($\varepsilon = 23$ Co–CeO_2/SnO_2 Ni foam); V_1 is a semiconductor's flat band potential, such as Co–CeO_2/SnO_2, ε^0 is the vacuum permittivity; V is the applied bias at the electrode; and N_d is the carrier density. Fig. 8d displays the Ragone plots and the as-prepared electrode's matching linear fits. The electrode made of Co–CeO_2/SnO_2 has a measured mass of 2 mg. For Co–CeO_2/SnO_2 electrodes, Fig. 8f displays the derived $1/C^2-V$ MS curves. The electrodes are n-

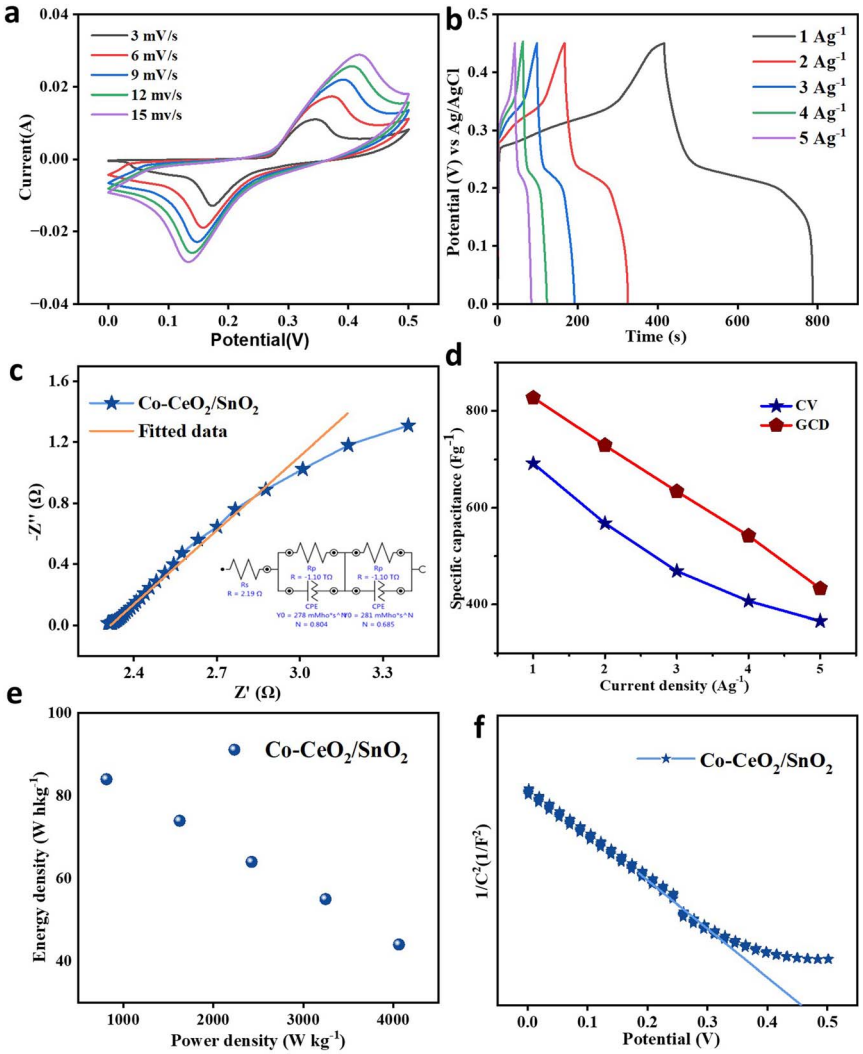

Fig. 8 (a) CV curve of Co–CeO_2/SnO_2; scan rate: 3 to 15 mV s^{-1} (b) GCD contrast curves at the current density of 1 to 6 A g^{-1}. (c) ESI contrast curve of Co–CeO_2/SnO_2. (d) Specific capacitance *vs.* current density. (e) Ragone plot of Co–CeO_2/SnO_2. (f) Mott–Schottky curve of Co–CeO_2/SnO_2.

Table 4 Comparison of specific capacitance, energy density, power density, and EIS for Co–CeO_2/SnO_2

CV—specific capacitance		GCD—specific capacitance				
Scan rate (mV s^{-1})	Capacitance (F g^{-1})	Current (A g^{-1})	Capacitance (F g^{-1})	Power density (W h kg^{-1})	Energy density (W kg^{-1})	ESI (Ω)
3	692	1	827	813	84	2.19
6	568	2	729	1625	74	
9	469	3	634	2425	64	
12	407	4	542	3246	55	
15	366	5	433	4062	44	
After cycling						
3	321	1	466	840	49	2.32

type semiconductors with electrons as the predominant carriers, according to MS plots, which have positive slopes.[61]

Fig. S4a† shows the after-cycle CV curve of Co–CeO_2/SnO_2 at a scan rate of 3 mV s^{-1}. In Fig. S4b,† the GCD contrast curve at a current density of 1 A g^{-1} is plotted. Fig. S4c† shows the ESI contrast curve of Co–CeO_2/SnO_2, and Fig. S4d† shows the capacity retention plot. After cycling, there is a slight drop in CV current and GCD potential compared to the initial values, indicating good retention of the material.

Table 5 Comparison of the specific capacitance of Ni-foam-based supercapacitor probes

Materials	Electrolyte	Current density ($A\ g^{-1}$)	Specific capacitance ($F\ g^{-1}$)	Reference
SnO_2/graphene	1 M Na_2SO_4	1	347.3	62
Ni–CeO_2	6 M KOH	1	370	63
Ni_3S_4/CeO_2	2 M KOH	2	1364	64
$NiSnO_3$/graphene	3 M KOH	1	570	65
Mn_3O_4–SnO_2	1 M Na_2SO_4	1	355	66
AC/GO/TiO_2–Zn	3 M KOH	2.5	1491.6	67
Cr–CeO_2	2 M KOH	1	42.6	61
GP–CoFe	2 M KOH	1	169	68
ZnO/SnO_2:rGO	1 M Na_2SO_4	3	3238	69
Sn/SnO_2	1 M H_2SO_4	1	508	58
Co–CeO_2/SnO_2	4 M KOH	1	827	Present study

7. Conclusion

In this work, Co–CeO_2/SnO_2, Co–CeO_2, and Co–SnO_2 nanocomposites were prepared in water and H_2O/Pr^iOH (70/30% v/v), and a photochemical reduction technique was used to successfully characterise the samples. Surface removal and photocatalytic reduction of Co(III) were investigated using sacrificial reactions with adjusted catalyst dosages and pH media. Increasing the surface contact between compounds and impurities increases the reduction properties at a low pH of the solution. CeO_2/SnO_2 has a higher rate constant ($0.0625\ min^{-1}$) for the reduction of Co(III) to Co(II) than the former. The stability of Co–CeO_2/SnO_2 ternary compounds was demonstrated by the XRD pattern and photocatalytic degradation of Co(III) probes, which can withstand three cycles. It is non-toxic, low-cost, and has properties evidenced by its electrical conductivity, which obtained a specific capacitance value of 692 $F\ g^{-1}$ at 3 $mV\ s^{-1}$ from CV and 827 $F\ g^{-1}$ at 1 $A\ g^{-1}$ from GCD, which is superior among metal oxide semiconductors.

Data availability

The data supporting the present results can be obtained from the corresponding author upon reasonable request.

Author contributions

The research work was designed under the guidance of Prof. K. Anbalagan; all experiments were carried out by R. Silambarasan; the article was reviewed and the electrochemical experiments were supported by Uttej Siva Sai Sundar Perisetti and S. Pavalamalar.

Conflicts of interest

There are no conflicts of interest to declare.

Acknowledgements

The authors thank the Central Instrumentation Facility (CIF), Pondicherry University, for providing the instrumental facility.

References

1 M. Pavel, C. Anastasescu, R. N. State, A. Vasile, F. Papa and I. Balint, *Catalysts*, 2023, **13**(2), 380, DOI: 10.3390/catal13020380.
2 F. Fresno, M. D. Hernández-Alonso, D. Tudela, J. M. Coronado and J. Soria, *Appl. Catal., B*, 2008, **84**, 598–606, DOI: 10.1016/j.apcatb.2008.05.015.
3 A. H. Navidpour, S. Abbasi, D. Li, A. Mojiri and J. L. Zhou, *Catalysts*, 2023, **13**(2), 232, DOI: 10.3390/catal13020232.
4 H. Eskandarloo, A. Badiei and M. A. Behnajady, *Ind. Eng. Chem. Res.*, 2014, **53**, 7847–7855, DOI: 10.1021/ie403460d.
5 J. Roh, S. H. Hwang and J. Jang, *J. Mater. Chem. A*, 2014, **2**, 16429–16433, DOI: 10.1039/c4ta03087g.
6 G. Nisha and P. Bhattacharya, *J. Mater. Chem. C*, 2023, **11**, 13503–13517, DOI: 10.1039/d3tc02074f.
7 Y. J. Seok, G. Nisha and P. Bhattacharya, *Adv. Funct. Mater.*, 2022, **32**(19), 2112509, DOI: 10.1002/adfm.202112509.
8 Y. S. S. Sarma, G. Nisha and P. Bhattacharya, *J. Alloys Compd.*, 2022, **62**(6), 1918–1926, DOI: 10.1002/pen.25975.
9 F. Fu and Q. Wang, *J. Environ. Manage.*, 2011, **92**, 407–418, DOI: 10.1016/j.jenvman.2010.11.011.
10 M. Imtiaz and M. K. Verma, *Int. J. Creat. Res. Thoughts*, 2022, **10**, 2320–2882.
11 L. Y. Ozer, C. Garlisi, H. Oladipo, M. Pagliaro, S. A. Sharief, A. Yusuf, S. Almheiri and G. Palmisano, *J. Photochem. Photobiol., C*, 2017, **33**, 132–164, DOI: 10.1016/j.jphotochemrev.2017.06.003.
12 J. S. Algethami, M. S. Hassan, T. Amna, F. A. Sheikh, M. A. M. Alhamami, A. F. Seliem, M. Faisal and H. Y. Kim, *Nanomaterials*, 2023, **13**, 1001, DOI: 10.3390/nanol3061001.
13 Z. Li, P. Graziosi and N. Neophytou, *Crystals*, 2022, **12**, 1–11, DOI: 10.3390/cryst12111591.
14 E. Kusmierek, *Catalysts*, 2020, **10**, 1435, DOI: 10.3390/catal10121435.
15 S. Grushevskaya, I. Belyanskaya and O. Kozaderov, *Materials*, 2022, **15(14)**, 4915, DOI: 10.3390/ma15144915.
16 L. Zhang, H. H. Mohamed, R. Dillert and D. Bahnemann, *J. Photochem. Photobiol., C*, 2012, **13**, 263–276, DOI: 10.1016/j.photochemrev.2012.07.002.

17 M. Javed, S. Iqbal, M. A. Qamar, M. Shariq, I. A. Ahmed, A. BaQais, H. Alzahrani, S. K. Ali, N. A. Masmali, T. M. Althagafi and M. S. Khan, *Crystals*, 2023, **13**, 1–17, DOI: **10.3390/cryst13020163**.

18 D. Toloman, A. Popa, M. Stefan, T. D. Silipas, R. C. Suciu, L. Barbu-Tudoran and O. Pana, *Opt. Mater.*, 2020, **110**, 110472, DOI: **10.1016/j.optmat.2020.110472**.

19 D. Toloman, A. Popa, M. Stefan, T. D. Silipas, R. C. Suciu, L. Barbu-Tudoran and O. Pana, *Opt. Mater.*, 2020, **110**, 110472, DOI: **10.1016/j.optmat.2020.110472**.

20 G. Killivalavan, B. Sathyaseelan, G. Kavitha, I. Baskarann, K. Senthilnathan, D. Sivakumar, N. Karthikeyan, E. Manikandan and M. Maaza, *MRS Adv.*, 2020, **5**, 2503–2515, DOI: **10.1557/adv.2020.296**.

21 P. H. Patil, V. V. Kulkarni and S. A. Jadhav, *J. Compos. Sci.*, 2022, **6**(12), 363, DOI: **10.3390/jcs6120363**.

22 K. Adaikalam, S. Ramesh, P. Santhoshkumar, H. S. Kim, H. C. Park and H. S. Kim, *Int. J. Energy Res.*, 2022, **46**, 4494–4505, DOI: **10.1021/acsomega.2c06010**.

23 A. K. Singh, D. Sarkar, K. Karmakar, K. Mandal and G. G. Khan, *ACS Appl. Mater. Interfaces*, 2016, **8**, 20786–20792, DOI: **10.1021/acsami.6b05933**.

24 B. Shunmugapriya, A. Rose, T. Maiyalagan and T. Vijayakumar, *Nanotechnology*, 2020, **31**(28), 285401, DOI: **10.1088/1361-6528/ab824e**.

25 L. B. Kong, C. Lu, M. C. Liu, Y. C. Luo, L. Kang, X. Li and F. C. Walsh, *Electrochim. Acta*, 2014, **115**, 22–27, DOI: **10.1039/c4ta00582a**.

26 X. Wang, Z. Wang, D. Peak, Y. Tang, X. Feng and M. Zhu, *ACS Earth Space Chem.*, 2018, **2**, 387–398, DOI: **10.3390/nano10020254**.

27 S. S. M. Hassan, A. H. Kamel, A. A. Hassan, A. E. G. E. Amr, H. A. El-Naby and E. A. Elsayed, *Nanomaterials*, 2020, **10**, 1–14, DOI: **10.1021/acsearthspacechem.7b00154**.

28 E. N. Zare, M. M. Lakouraj and A. Ramezani, *Adv. Polym. Technol.*, 2015, **34**, 1–11, DOI: **10.1002/adv.21501**.

29 D. Venkatesh, S. Pavalamalar, R. Silambarasan and K. Anbalagan, *J. Inorg. Organomet. Polym. Mater.*, 2022, **32**, 2712–2728, DOI: **10.1007/s10904-022-02304-1**.

30 R. Silamabarasan, S. Pavalamalar, U. S. S. S. Perisetti and K. Anbalagan, *Ionics*, 2023, **30**, 383–398, DOI: **10.1007/s11581-023-05288-1**.

31 D. Venkatesh, R. Silambarasan and K. Anbalagan, *J. Mater. Sci.: Mater. Electron.*, 2022, **33**, 20678–20695, DOI: **10.1007/s10854-022-08879-2**.

32 N. K. Mishra, C. Kumar, A. Kumar, M. Kumar, P. Chaudhary and R. Singh, *Mater. Sci. Polym.*, 2015, **33**, 714–718, DOI: **10.1515/msp-2015-0101**.

33 Y. Chen, M. Zhou, Z. Dong, A. Natan, S. Chen, Y. Yang, X. Huang and Y. Yang, *Appl. Phys. A: Mater. Sci. Process.*, 2020, **126**, 1–11, DOI: **10.1007/s00339-019-3158-8**.

34 N. H. Lam, R. P. Smith, N. Le, C. T. T. Thuy, M. S. Tamboli, A. M. Tamboli, S. Alshehri, M. M. Ghoneim, N. T. N. Truong and J. H. Jung, *Crystals*, 2022, **12**(4), 566, DOI: **10.3390/cryst12040566**.

35 M. Sridharan, T. Maiyalagan, G. Panomsuwan and R. Techapiesancharoenkij, *Catalysts*, 2022, **12**(1), 6, DOI: **10.3390/catal12010006**.

36 V. Kumar, K. Singh, J. Sharma, A. Kumar, A. Vij and A. Thakur, *J. Mater. Sci.: Mater. Electron.*, 2017, **28**, 18849–18856, DOI: **10.1007/s10854-017-7836-z**.

37 S. Asaithambi, P. Sakthivel, M. Karuppaiah, Y. Hayakawa, A. Loganathan and G. Ravi, *Appl. Phys. A: Mater. Sci. Process.*, 2020, **126**, 1–12, DOI: **10.1007/s00339-020-3441-8**.

38 V. Fernandes, J. J. Klein, N. Mattoso, D. H. Mosca, E. Silveira, E. Ribeiro, W. H. Schreiner, J. Varalda and A. J. A. De Oliveira, *Phys. Rev. B: Condens. Matter Mater. Phys.*, 2007, **75**, 1–5, DOI: **10.1103/PhysRevB.75.121304**.

39 A. Hezam, K. Namratha, Q. A. Drmosh, D. Ponnamma, J. Wang, S. Prasad, M. Ahamed, C. Cheng and K. Byrappa, *ACS Appl. Nano Mater.*, 2020, **3**, 138–148, DOI: **10.1021/acsanm.9b01833**.

40 S. Prakash Bharti, E. Singh and U. Kumar, *Nanosci. Nanotechnol. Res.*, 2017, **4**, 115–119, DOI: **10.12691/nnr-4-3-5**.

41 V. Garg and H. Sharma, *J. Emerg. Technol. Innov. Res.*, 2018, **5**(10), 656–665, DOI: **10.1729/Journal.24271**.

42 W. H. Zhang and W. De Zhang, *Sens. Actuators, B*, 2008, **134**, 403–408, DOI: **10.1016/j.snb.2008.05.015**.

43 K. R. Jawaher, R. Indirajith, S. Krishnan, R. Robert, S. K. K. Pasha, K. Deshmukh and S. J. Das, *J. Sci.: Adv. Mater. Devices*, 2018, **3**, 139–144, DOI: **10.1016/j.snb.2008.05.015**.

44 Y. Huang, Y. Lu, Y. Lin, Y. Mao, G. Ouyang, H. Liu, S. Zhang and Y. Tong, *J. Mater. Chem. A*, 2018, **6**, 24740–24747, DOI: **10.1016/j.jsamd.2018.03.006**.

45 R. N. Mariammal, K. Ramachandran, B. Renganathan and D. Sastikumar, *Sens. Actuators, B*, 2012, **169**, 199–207, DOI: **10.1016/j.snb.2012.04.067**.

46 C. S. Ponseca, E. M. Hutter, P. Piatkowski, B. Cohen, T. Pascher, A. Douhal, A. Yartsev, V. Sundström and T. J. Savenije, *J. Am. Chem. Soc.*, 2015, **137**, 16043–16048, DOI: **10.1039/c8ta06565a**.

47 C. Zhou, S. Wang, Z. Zhao, Z. Shi, S. Yan and Z. Zou, *Adv. Funct. Mater.*, 2018, **28**, 1801214, DOI: **10.1002/adfm.201801214**.

48 S. Phokha, S. Pinitsoontorn, P. Chirawatkul, Y. Poo-arporn and S. Maensiri, *Nanoscale Res. Lett.*, 2012, **7**, 1–13.

49 S. Usharani and V. Rajendran, *Eng. Sci. Technol. an Int. J.*, 2016, **19**, 2088–2093, DOI: **10.1016/j.jestch.2016.10.008**.

50 N. Wan, X. Lu, Y. Wang, W. Zhang, Y. Bai, Y. S. Hu and S. Dai, *Sci. Rep.*, 2016, **6**, 18978, DOI: **10.1038/srep18978**.

51 M. Kumar, V. Bhatt, A. C. Abhyankar, J. Kim, A. Kumar, S. H. Patil and J. H. Yun, *Sci. Rep.*, 2018, **8**, 1–13, DOI: **10.3906/fiz-1405-4**.

52 Y. Li, W. Li, F. Liu, M. Li, X. Qi, M. Xue, Y. Wang and F. Han, *J. Nanopart. Res.*, 2020, **22**, 122, DOI: **10.1007/s11051-020-04860-4**.

53 A. A. Farghali, W. M. A. El Rouby and A. Hamdedein, *Res. Chem. Intermed.*, 2017, **43**, 7171–7192, DOI: **10.1007/s11164-017-3067-4**.

54 M. Gupta, S. Tyagi and N. Kumari, *J. Mater. Sci.: Mater. Electron.*, 2022, **33**, 7838–7852, DOI: **10.1007/s10854-022-07935-1**.
55 G. Nisha, K. S. Ranjan, T. Mishra and P. Bhattacharya, *J. Mater. Chem. A*, 2022, **10**, 15794–15810, DOI: **10.1039/d2ta04061a**.
56 S. Nayak, A. A. Kittur and S. Nayak, *J. Electron. Mater.*, 2023, **52**, 1437–1447, DOI: **10.1007/s11664-022-10099-7**.
57 M. Barazandeh and S. H. Kazemi, *Sci. Rep.*, 2022, **12**, 1–13, DOI: **10.1038/s41598-022-08691-2**.
58 T. Su, Y. Yang, Y. Na, R. Fan, L. Li, L. Wei, B. Yang and W. Cao, *ACS Appl. Mater. Interfaces*, 2015, **7**, 3754–3763, DOI: **10.1021/am5085447**.
59 A. Durairaj, T. Sakthivel, S. Ramanathan and S. Vasanthkumar, *ACS Omega*, 2019, **4**, 6476–6485, DOI: **10.1021/acsomega.8b03279**.
60 T. Wang, J. Liu, P. Wu, C. Feng, D. Wang, H. Hu and G. Xue, *J. Mater. Chem. A*, 2020, **8**, 16590–16598, DOI: **10.1039/c9ta13902h**.
61 B. Veena, S. Pavithra, M. Seetha, A. Sakunthala and Y. Masuda, *AIP Adv.*, 2022, **12**, 125310, DOI: **10.1063/5.0130499**.
62 Y. Wang, Y. Liu and J. Zhang, *J. Nanopart. Res.*, 2015, **17**, 1–10, DOI: **10.1038/srep09164**.
63 M. Ponnar, K. Pushpanathan, R. Santhi and S. Ravichandran, *J. Mater. Sci.: Mater. Electron.*, 2020, **31**, 12661–12677, DOI: **10.1007/s10854-020-03816-7**.
64 F. Feng-zhi, M. Mu-tian, C. Wei-jie, C. Yong-li, W. Yuan-hao and Z. Jing-hui, *J. Saudi Chem. Soc.*, 2022, **26**, 101530, DOI: **10.1016/j.jscs.2022.101530**.
65 P. E. Saranya and S. Selladurai, *J. Mater. Sci.*, 2018, **53**, 16022–16046, DOI: **10.1007/s10853-018-2742-1**.
66 B. G. S. Raj, R. Angulakshmi, N. Baskaran, J. J. Wu, S. Anandan and M. Ashokkumar, *J. Appl. Electrochem.*, 2020, **50**, 609–619, DOI: **10.1007/s10800-020-01421-4**.
67 S. Veeresh, H. Ganesha, H. Vijeth and H. Devendrappa, *J. Alloys Compd.*, 2023, **952**, 169907, DOI: **10.1016/j.jallcom.2023.169907**.
68 D. T. Tung, L. T. T. Tam, H. T. Dung, N. T. Dung, H. T. Ha, N. T. Dung, T. Hoang, T. D. Lam, T. V. Thu, D. T. Chien, P. N. Hong, P. N. Minh, N. V. Quynh and L. T. Lu, *J. Electron. Mater.*, 2020, **49**, 4671–4679, DOI: **10.1007/s11664-020-08165-z**.
69 V. Shanmugapriya, S. Arunpandian, G. Hariharan, S. Bharathi, B. Selvakumar and A. Arivarasan, *J. Alloys Compd.*, 2023, **935**, 167994, DOI: **10.1016/j.jallcom.2022.167994**.